Synchronous rise of African C$_4$ ecosystems 10 million years ago in the absence of aridification

Pratigya J. Polissar [1]*, Cassaundra Rose [2]*, Kevin T. Uno [1], Samuel R. Phelps [2] and Peter deMenocal[1,2]

Grasslands expanded globally during the late Cenozoic and the development of these ecosystems shaped the evolution of many faunal groups, including our hominin ancestors. The emergence of these ecosystems has been dated in many regions, but the origins of the iconic African C$_4$ savannah grasslands remain poorly known, as do the causal factors that led to their establishment. Here we document their origins with the distinct carbon isotope signature from the hot-, arid- and low-CO$_2$-adapted C$_4$ grasses that dominate modern savannahs and grasslands. We use the carbon isotope values of leaf-wax molecules in deep-sea drill cores to measure the rise of African C$_4$ ecosystems. We also reconstruct African palaeohydroclimate change from leaf-wax hydrogen isotope values and dust deposition rates in these cores. We find that C$_4$-dominated ecosystems expanded synchronously across Northwestern and East Africa after 10 million years ago. This was not accompanied by substantial changes in palaeohydrology or dust deposition, precluding aridification as a causal factor. The expansion of C$_4$ grasses was coincident, however, with dramatic high-latitude cooling and increased pole–Equator temperature gradients. We suggest that declining atmospheric CO$_2$ levels were a direct cause of the C$_4$ grassland expansion.

Plants that use the C$_4$ pathway, including savannah grasses, account for more than one-quarter of terrestrial primary productivity[1] and represent 40% of sub-Saharan African vegetation cover[2]. The anatomical and biochemical modifications that define this unique carbon fixation pathway first evolved near 32–25 million years ago (Ma)[3,4] but marked global expansion of C$_4$ vegetation did not occur until the late Miocene (10–6 Ma)[5,6]. The late Miocene emergence of C$_4$ grasslands was associated with mammalian faunal evolution and adaptive responses (hypsodonty), including changes in ancestral hominin behaviour and diet[7]. However, little is known about the antiquity of Northwest African C$_4$ savannah grasslands, particularly their relationship with East African vegetation changes, the palaeohydrological context of their expansion, the association with Saharan dust activation and the principal mechanism that led to the emergence of this remarkably important ecosystem.

We date the emergence and expansion of C$_4$ grassland ecosystems across Northwest and East Africa using continuous, well-dated, deep-sea drilling sedimentary sequences spanning the latest Oligocene to present (24.3–0 Ma, Supplementary Table 1). The preservation of terrestrial plant-wax molecules in these sediments affords the opportunity to reconstruct the abundance of C$_4$ vegetation, a tracer for the savannah biome in modern Africa. Molecular carbon isotope compositions (δ^{13}C) of plant-waxes record the proportion of C$_4$ plants (warm-season savannah grasses) versus C$_3$ plants (trees, shrubs, herbs and cool-season grasses) on the landscape (Fig. 1). Their hydrogen isotope compositions (δD) can also be used to reconstruct the hydrogen isotope composition of rainfall, a sensitive indicator of rainfall amount in modern Africa[8,9]. Wind delivery of these compounds from the continent provides an integrated, spatially averaged view of regional ecosystem evolution. We also evaluate these African palaeovegetation and palaeohydrological records in the context of changes in the Saharan desert dust flux.

We analysed plant-wax n-alkane δ^{13}C and δD values from drill cores offshore of equatorial West Africa (ODP Site 959) and Northwest Africa (ODP Site 659), and report δD analyses from cores off East Africa (DSDP Sites 235 and 241) in combination with previously published δ^{13}C analyses[10]. Sites 659 and 959 span a large rainfall gradient that is closely mirrored by the latitudinal vegetation progression from wet equatorial rainforest (C$_3$ plants) through dry savannah (C$_4$ plants) to arid subtropical desert (Fig. 1). Comparison of the plant-wax records from these two sites captures the emergence of the modern vegetation and hydrologic gradient. Sites 235 and 241 in the Somali Basin record the evolution of the East African savannah and climate[10].

Onset of African C$_4$ ecosystem expansion at 10 Ma

Plant-wax δ^{13}C values between 25 and 10 Ma indicate that Northwest and East African vegetation was dominated by C$_3$ ecosystems at the regional scale, with no major isotope trends or differences between equatorial (sites 959, 235 and 241) and West African (Site 659) locations (Fig. 2a–c). At 10 Ma, however, the δ^{13}C values of C$_{31}$ n-alkanes increased synchronously at all sites, indicating the rise of C$_4$ vegetation cover across Northwest and East Africa. The abrupt and larger δ^{13}C increase in the C$_{35}$ n-alkane at ~10.5 Ma (sites 659 and 959) and ~9.9 Ma (sites 235 and 241) sensitively dates the onset of C$_4$ vegetation expansion, as this molecule is known to be preferentially abundant in African C$_4$ graminoids (grasses) compared with savannah or rainforest trees[11]. Factors such as aridity and temperature may also determine the relative abundance of long-chain n-alkanes; however, our combined leaf-wax abundance and δ^{13}C data indicate that the increasing δ^{13}C signature of the C$_{35}$ n-alkane dates the onset of C$_4$ ecosystem expansion (Supplementary Discussion 2.1, Supplementary Fig. 11). This C$_4$ expansion also begins at ~10 Ma in a plant-wax δ^{13}C record from Site 231 in the Gulf of Aden, off northeast Africa[12]. Carbon isotope values at Site 659 (off northwest Africa) and sites 235 and 241 (off East Africa) increase by over 7‰ from 10 Ma to present, interpreted as a rise to 60% C$_4$ vegetation cover across North and East Africa.
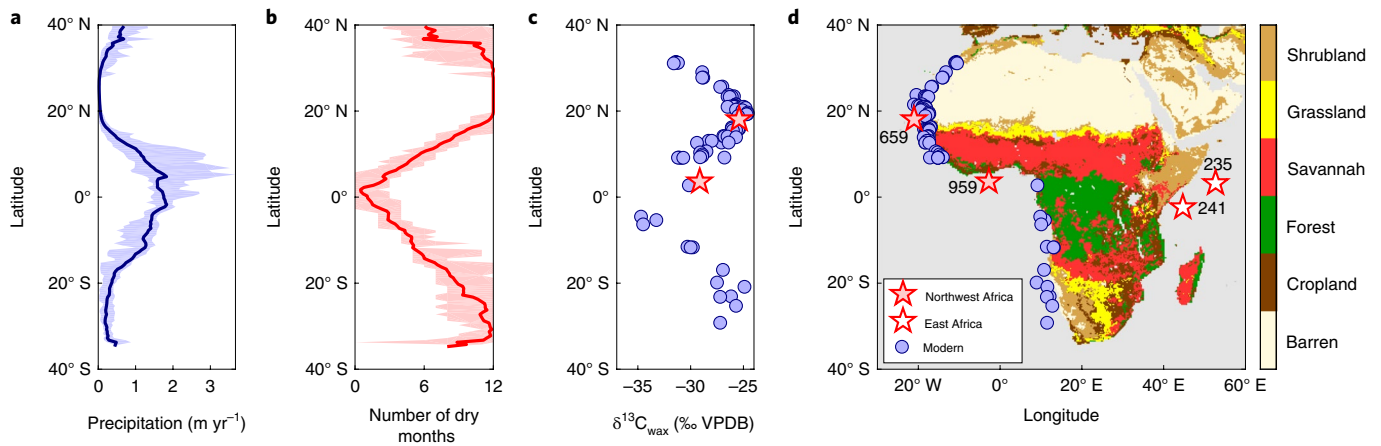
Fig. 1 | Latitudinal patterns of modern African rainfall, carbon isotope values of long-chain plant-waxes and vegetation cover. a, Annual rainfall. **b**, The number of months per year with less than 5 cm of rainfall. **c**, The dominance of C_4 grasses in grassland and savannah ecosystems is reflected in the more positive $\delta^{13}C$ values of n-C_{31} alkane plant-waxes in modern marine sediments. **d**, These factors control the occurrence of arid (xeric shrubland, grassland and savannah) and humid (forest) ecosystems. Median (line) and range (shading) of rainfall statistics averaged for 20° W to 25° E were calculated from ref. [30]. Data for vegetation cover are from ref. [31], and modern marine sediment data are from refs. [32–34]. The legend in **d** also applies to **c**.
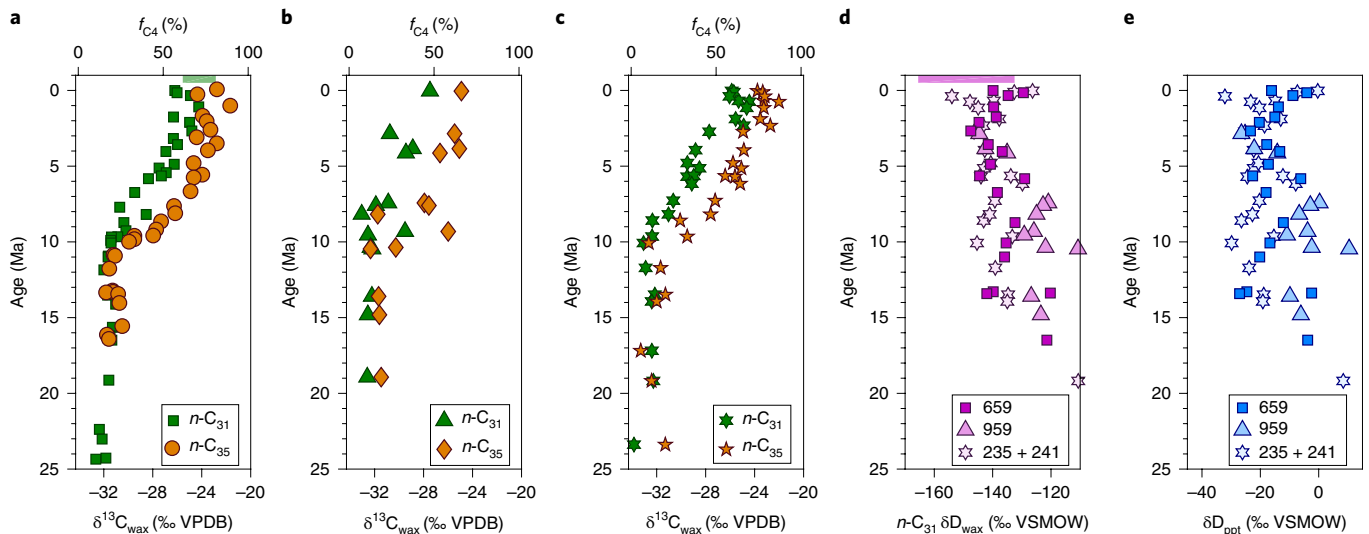

Fig. 2 | Plant-wax records of Neogene vegetation and hydrologic change. a–c, Plant-wax $\delta^{13}C$ values corrected for atmospheric $\delta^{13}C$ values for sites 659 (**a**), 959 (**b**) and 235 and 241 combined (**c**). The fraction of C_4 vegetation, f_{C4}, for n-C_{31} calculated from modern African vegetation endmembers is plotted on the top x axis. **d**, Plant-wax δD_{wax} values were corrected for seawater δD. **e**, Precipitation δD_{ppt} was calculated using a vegetation-dependent fractionation factor (described in the Methods). The bars at the top of **a** and **d** indicate the range of n-C_{31} $\delta^{13}C_{wax}$ and δD_{wax} values during both the past 120 kyr and the Pliocene at Site 659 (refs. [35,36]).

The emergence of widespread C_4 vegetation had a significant and immediate impact on the diets of large mammals in East Africa: proboscideans and equids quickly added C_4 vegetation to their diets, with some equids consuming significant amounts of C_4 plants (>65% of diet) by 9.9 Ma and rhinoceratids and bovids following suit by 9.6 Ma (ref. [13]). Ultimately, many African mammalian lineages adopted diets based entirely or significantly on C_4 vegetation[13,14], including most hominin lineages[7,15].

Hydrologic change did not drive C_4 expansion

What triggered the replacement of C_3 plants with predominantly C_4 grasses? The C_4 photosynthesis pathway is more efficient under low partial pressures of CO_2 (p_{CO_2}) and high growing season temperatures, and C_4 plants are favoured under conditions of lower effective rainfall and highly seasonal precipitation[16–18]. To evaluate whether

changes in growing season hydrology drove the C_4 grassland expansion, we measured the hydrogen isotope ratios of long-chain plant-wax n-alkanes (δD_{wax}) at sites 235, 241, 659 and 959 (Fig. 2d). Modern δD_{wax} values from Northwest Africa are strongly controlled by the amount of rainfall[8,9], and ancient δD_{wax} tracks Northwest and East African rainfall on orbital and millennial timescales[9]. Rainfall δD values (δD_{ppt}) show no secular trends or changes in variability from the middle Miocene to the present (Fig. 2e, Supplementary Figs. 9 and 10). The observed rainfall δD_{ppt} variability (20–30‰) is comparable to orbitally driven cycles observed in Pliocene to modern North African records (Supplementary Fig. 9), suggesting that similar hydroclimate variability extended to at least 15 Ma. The absence of significant changes in both the mean and range of our δD_{wax} values indicates that growing season hydroclimate was largely stable across the C_4 transition.

flux = fraction dust*DBD*sedrate (g/cm2/kyr)
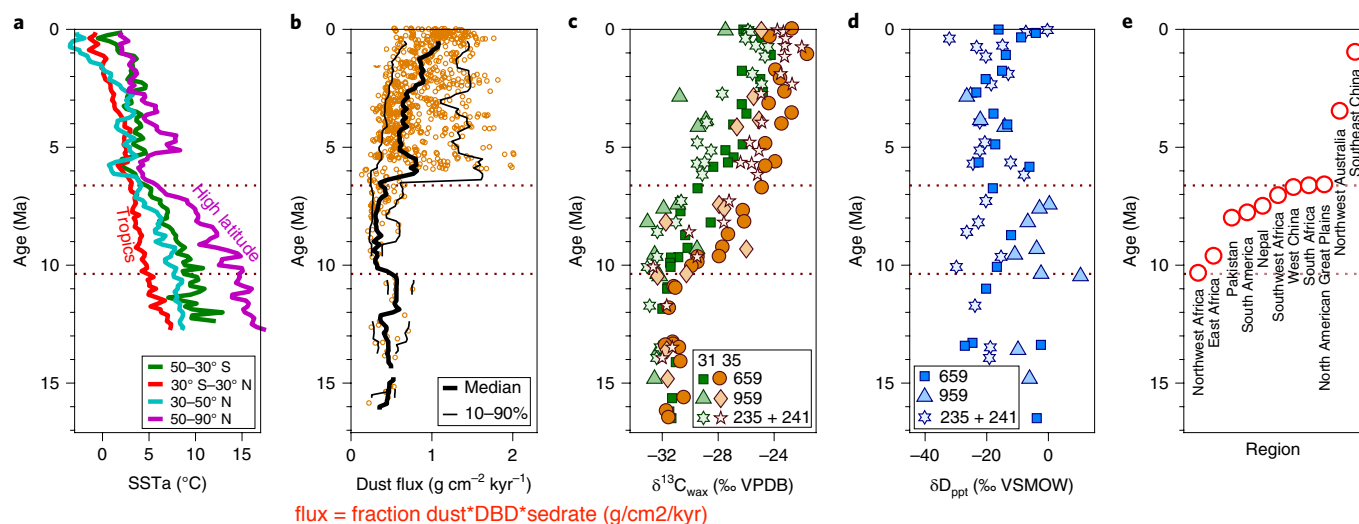
Fig. 3 | Evolution of global SST and African dust flux compared with C₄ expansion and African hydrologic change. a, SST anomalies (SSTa) indicate late Miocene cooling and strengthening latitudinal gradients that establish the modern latitudinal distributions (see Methods). **b**, Dust flux off Northwest Africa measured at Site 659 increases at the end of the Miocene, post-dating the major phase of C₄ expansion (**c**). **d**, No apparent change in rainfall δD$_{ppt}$ accompanied the onset or expansion of C₄ ecosystems in Northwest or East Africa. **e**, The onset of C₄ expansion across the globe occurs during the main phase of cooling and strengthening of SST gradients. The timing of C₄ expansion is indicated by the dotted horizontal lines (Supplementary Discussion 2.3).

We further investigate possible changes in aridity with a newly calculated record of dust flux from Northwest African Site 659. Dust fluxes increased markedly from 7 to 6 Ma, well after the onset and major expansion phase of C₄ vegetation (10–7 Ma) and the earliest evidence for sand dunes in the Sahara (>7 Ma)[19] (Fig. 3c). Increased fluxes may indicate aridification, but probably also reflect increased wind strength and transport[20]. The dust flux increase clearly post-dates the onset of C₄ grass expansion, supporting the hydrogen isotope evidence that this vegetation shift was not due to regional aridification.

Palaeobotanical evidence suggests that C₃ wooded grassland and woodland ecosystems dominated the North and East African landscapes before C₄ grasses expanded (Supplementary Discussion 2.2). These studies indicate heterogeneous ecosystems were present, including significant C₃ grass abundances[12,21]. Hence, it is likely that C₄ grasses would have replaced C₃ grasses in existing open and dry environments[22]. It is unlikely that C₄ grasses would have replaced rainforests or other, mesic ecosystems as C₄ plants are shade-intolerant[23]. Fire is important in maintaining modern C₄ savannahs and has been suggested as a driver for late Miocene C₄ grass expansion[24]. However, charred grass cuticle is consistently found in post-16 Ma sediments of the Niger Delta[25], indicating that grass fires greatly predated the expansion of C₄ grasses. Fire was therefore not a direct cause, but could have been a positive feedback to C₄ grass expansion. The palaeobotanical evidence, along with our δD$_{ppt}$ record, suggests that C₄ grasses expanded into already seasonally dry ecosystems without any substantial hydroclimate change.

Global synchronization of C₄ ecosystem expansion

What then led to the establishment of the modern C₄ ecosystems in Africa? We suggest that decreasing atmospheric CO₂ ultimately spurred the emergence of C₄ vegetation in Northwest and East Africa. Although published p_{CO_2} reconstructions do not indicate a CO₂ decrease at this time[26], emerging records suggest a decline during the late Neogene, around the time that C₄ plants began increasing in North and East Africa[27,28]. Herbert et al.[29] also argue for a CO₂ decline at this time based on the latitudinal pattern of late Neogene sea surface temperature (SST) cooling.

We compared detailed marine cooling records with our North African palaeovegetation proxy data to explore this proposed relationship (Fig. 3a). Global average SSTs declined nearly continuously between 12 and 6 Ma and cooling was enhanced at high latitudes, consistent with declining CO₂ levels and high-latitude feedbacks. We posit that declining CO₂ levels reached the threshold at which C₄ grasses gained a competitive advantage, first in the warm tropics such as North and East Africa, and later in the subtropics—as proposed in earlier studies[5,16]. In this scenario, middle Miocene temperatures and rainfall patterns in Northwest and East Africa were close to a threshold at which small CO₂ decreases conferred critical advantages to C₄ plants. A continued CO₂ decline progressively crossed this competitive threshold in other wetter and/or cooler regions, leading to the asynchronous onsets of C₄ expansion observed globally (Fig. 3e). The increased dust flux from Northwest Africa after 6 Ma probably reflects increased wind strength from intensified meridional temperature gradients[20].

Our vegetation reconstructions constrain the timing of C₄ vegetation expansion across Northwest and East Africa to ~10 Ma. Our plant-wax hydrogen isotope and dust flux records indicate this event was not associated with regional palaeohydrologic changes. The most parsimonious conclusion is that declining CO₂ levels during the late Miocene conferred photosynthetic advantages that promoted the expansion of C₄ vegetation across Northwest and East Africa, in agreement with pioneering studies[5,16]. Available palaeobotanical evidence suggests that C₄ grasses would have replaced C₃ grasses in existing open and dry environments. We cannot ascertain from our data alone when aridification of Northwest and East Africa began, and whether a proto-Saharan desert existed before the expansion of C₄ vegetation at ~10 Ma remains an open question.

Online content

Any methods, additional references, Nature Research reporting summaries, source data, statements of code and data availability and associated accession codes are available at https://doi.org/10.1038/s41561-019-0399-2.

References

1. Still, C. J., Berry, J. A., Collatz, G. J. & DeFries, R. S. Global distribution of C_3 and C_4 vegetation: carbon cycle implications. *Glob. Biogeochem. Cycles* **17**, 1006 (2003).
2. Still, C. J. & Powell, R. L. in *Isoscapes: Understanding Movement, Pattern, and Process on Earth Through Isotope Mapping* (eds West, J. B. et al.) 179–193 (Springer Netherlands, 2010).
3. Christin, P.-A. et al. Oligocene CO_2 decline promoted C_4 photosynthesis in grasses. *Curr. Biol.* **18**, 37–43 (2008).
4. Vicentini, A., Barber, J. C., Aliscioni, S. S., Giussani, L. M. & Kellogg, E. A. The age of the grasses and clusters of origins of C_4 photosynthesis. *Glob. Change Biol.* **14**, 2963–2977 (2008).
5. Cerling, T. E. et al. Global vegetation change through the Miocene/Pliocene boundary. *Nature* **389**, 153–158 (1997).
6. Stromberg, C. A. E. Evolution of grasses and grassland ecosystems. *Annu. Rev. Earth Planet. Sci.* **39**, 517–544 (2011).
7. Sponheimer, M. et al. Isotopic evidence of early hominin diets. *Proc. Natl Acad. Sci. USA* **110**, 10513–10518 (2013).
8. Niedermeyer, E. M. et al. The stable hydrogen isotopic composition of sedimentary plant waxes as quantitative proxy for rainfall in the West African Sahel. *Geochim. Cosmochim. Acta* **184**, 55–70 (2016).
9. Tierney, J. E., Pausata, F. S. R. & deMenocal, P. B. Rainfall regimes of the Green Sahara. *Sci. Adv.* **3**, e1601503 (2017).
10. Uno, K. T., Polissar, P. J., Jackson, K. E. & deMenocal, P. B. Neogene biomarker record of vegetation change in eastern Africa. *Proc. Natl Acad. Sci. USA* **113**, 6355–6363 (2016).
11. Bush, R. T. & McInerney, F. A. Leaf wax *n*-alkane distributions in and across modern plants: implications for paleoecology and chemotaxonomy. *Geochim. Cosmochim. Acta* **117**, 161–179 (2013).
12. Feakins, S. J. et al. Northeast African vegetation change over 12 m.y. *Geology* **41**, 295–298 (2013).
13. Uno, K. T. et al. Late Miocene to Pliocene carbon isotope record of differential diet change among East African herbivores. *Proc. Natl Acad. Sci. USA* **108**, 6509–6514 (2011).
14. Cerling, T. E. et al. Dietary changes of large herbivores in the Turkana Basin, Kenya from 4 to 1 Ma. *Proc. Natl Acad. Sci. USA* **112**, 11467–11472 (2015).
15. Cerling, T. E. et al. Stable isotope-based diet reconstructions of Turkana Basin hominins. *Proc. Natl Acad. Sci. USA* **110**, 10501–10506 (2013).
16. Ehleringer, J. R., Cerling, T. E. & Helliker, B. R. C_4 photosynthesis, atmospheric CO_2, and climate. *Oecologia* **112**, 285–299 (1997).
17. Sankaran, M. et al. Determinants of woody cover in African savannas. *Nature* **438**, 846–849 (2005).
18. Lehmann, C. E., Archibald, S. A., Hoffmann, W. A. & Bond, W. J. Deciphering the distribution of the savanna biome. *New Phytol.* **191**, 197–209 (2011).
19. Schuster, M. et al. The age of the Sahara Desert. *Science* **311**, 821–821 (2006).
20. Mcgee, D., Broecker, W. S. & Winckler, G. Gustiness: the driver of glacial dustiness? *Quat. Sci. Rev. 29* **29**, 2340–2350 (2010).
21. Bonnefille, R. Cenozoic vegetation, climate changes and hominid evolution in tropical Africa. *Glob. Planet. Change* **72**, 390–411 (2010).
22. Sage, R. F., Wedin, D. A. & Li, M. in C_4 *Plant Biology* (eds Sage, R. F. & Monson, R. K.) 313–373 (Academic, 1999).
23. Sage, R. F. & Kubien, D. S. Quo vadis C_4? An ecophysiological perspective on global change and the future of C_4 plants. *Photosynth. Res.* **77**, 209–225 (2003).
24. Keeley, J. E. & Rundel, P. W. Fire and the Miocene expansion of C_4 grasslands. *Ecol. Lett.* **8**, 683–690 (2005).
25. Morley, R. J. & Richards, K. Gramineae cuticle: a key indicator of Late Cenozoic climatic change in the Niger Delta. *Rev. Palaeobot. Palynol.* **77**, 119–127 (1993).
26. Pagani, M., Arthur, M. A. & Freeman, K. H. Miocene evolution of atmospheric carbon dioxide. *Paleoceanography* **14**, 273–292 (1999).
27. Bolton, C. T. et al. Decrease in coccolithophore calcification and CO_2 since the middle Miocene. *Nat. Commun.* **7**, 10284 (2016).
28. Mejia, L. M. et al. A diatom record of CO_2 decline since the late Miocene. *Earth Planet. Sci. Lett.* **479**, 18–33 (2017).
29. Herbert, T. D. et al. Late Miocene global cooling and the rise of modern ecosystems. *Nat. Geosci.* **9**, 843–847 (2016).
30. Legates, D. R. & Willmott, C. J. Mean seasonal and spatial variability in gauge-corrected, global precipitation. *Int. J. Climatol.* **10**, 111–127 (1990).
31. Loveland, T. et al. *ISLSCP II IGBP DISCover and SiB Land Cover 1992-1993* (Oak Ridge National Laboratory Distributed Active Archive Center, 2009); https://doi.org/10.3334/ORNLDAAC/930
32. Collins, J. A. et al. Interhemispheric symmetry of the tropical African rainbelt over the past 23,000 years. *Nat. Geosci.* **4**, 42–45 (2011).
33. Rommerskirchen, F. et al. A north to south transect of Holocene southeast Atlantic continental margin sediments: relationship between aerosol transport and compound-specific δ13C land plant biomarker and pollen records. *Geochem. Geophys. Geosyst.* **4**, 1101 (2003).
34. Kuechler, R. R. *A Revised Orbital Forcing Concept of West African Climate and Vegetation Variability During the Pliocene and the Last Glacial Cycle.* PhD thesis, Univ. Bremen (2015).
35. Kuechler, R. R., Schefuss, E., Beckmann, B., Dupont, L. & Wefer, G. NW African hydrology and vegetation during the Last Glacial cycle reflected in plant-wax-specific hydrogen and carbon isotopes. *Quat. Sci. Rev.* **82**, 56–67 (2013).
36. Kuechler, R. R., Dupont, L. M. & Schefuss, E. Hybrid insolation forcing of Pliocene monsoon dynamics in West Africa. *Climate* **14**, 73–84 (2018).

Author contributions

C.R., P.J.P., K.T.U. and P.deM. conceived the study. C.R., P.J.P., K.T.U. and S.R.P. conducted the investigation. All authors wrote the manuscript. P.J.P. and P.deM. supervised the study.

Competing interests

The authors declare no competing interests.

Additional information

Supplementary information is available for this paper at https://doi.org/10.1038/s41561-019-0399-2.

Reprints and permissions information is available at www.nature.com/reprints.

Correspondence and requests for materials should be addressed to P.J.P. or C.R.

Publisher's note: Springer Nature remains neutral with regard to jurisdictional claims in published maps and institutional affiliations.

Methods

Sampling and chronology. Marine sediment core information for all sites is provided in Supplementary Table 1. Sediments from Site 659 are pelagic foraminifer–nannofossil oozes deposited outside the upwelling zone, away from turbidite fans and under the present Saharan air layer[37,38]. Site 959 is located on a small plateau in the Deep Ivorian Basin with foraminifer–nannofossil ooze from the Holocene–mid Miocene, and interbedded nannofossil chalk, diatomite and clay from the lower Oligocene to mid Miocene[39]. We revised the composite depth scales for Site 659[40–42] (Supplementary Table 2) and the calcareous nannofossil, planktonic foraminifera and palaeomagnetic datums for sites 659[41–43] and 959[44] according to updated age estimates[45–47] (Supplementary Methods 1.1 and Supplementary Tables 3 and 4). Supplementary Figs. 1 and 2 show the revised age–depth models and sedimentation rates for sites 659 and 959. Sampling information and updated age models for sites 235 and 241 were published previously[10].

Leaf-wax *n*-alkane biomarker extraction and quantification. ODP core samples were freeze-dried, and the outside of each sample removed before extraction. Samples were extracted by triplicate sonication with a solution of 9:1 dichloromethane:methanol (v/v), spiked with a recovery standard, purified with silica gel column chromatography and quantified by gas chromatography with flame ionization or mass-spectrometry detection (Supplementary Methods 1.2).

Compound-specific δ13C and δD analysis. Compound-specific δD and δ13C measurements were performed with a Thermo Delta V Plus Isotope Ratio Mass Spectrometer coupled to a Thermo Trace GC Ultra through a high-temperature pyrolysis or combustion interface, respectively. The GC oven temperature was held at 60 °C for 1.5 min, ramped at 15 °C min⁻¹ to 150 °C and held for 0 min, then ramped at 4 °C min⁻¹ to 320 °C and held for 10 min. δD measurements were automatically corrected by the operating software for isobaric contributions from H₃⁺ produced in the ion source of the mass spectrometer, using the H₃⁺ factor that was determined daily. Standard mixtures of *n*-alkanes and esters with known δ13C and δD isotope values (Mix A4, A5 and F8 purchased from A. Schimmelmann, Indiana Univ.) were regularly interspersed between sample measurements to calibrate the isotope measurements. Uncertainties (1 s.e.m.) for δ13C$_{wax}$ and δD$_{wax}$ were calculated using the method of ref. [48], and include both our analytical uncertainty and the uncertainty in realizing the VSMOW and VPDB reporting scales. Carbon and hydrogen isotope values are reported in Supplementary Table 5.

Corrections for atmospheric δ13C. Changes in the δ13C value of atmospheric CO₂ (δ13C$_{CO2}$) through time are recorded in δ13C$_{wax}$, and these changes must be accounted for to accurately quantify vegetation composition. We corrected our measured δ13C$_{wax}$ data for variations in δ13C$_{CO2}$ using the benthic foraminifera-based reconstruction of ref. [49] (3 Myr running average). We performed linear interpolation on the dataset to calculate δ13C$_{CO2}$ values at the same ages as our samples, calculated the photosynthetic fractionation of plant-wax isotope values from atmospheric CO₂ (ε_p, Eq. 1) and then calculated the corrected isotopic composition of plant-waxes (δ13C$_{wax,corr}$) to a pre-industrial atmospheric CO₂ composition of −6.5‰ VPDB (δ13C$_{CO2,PI}$, equation (2))[50]:

$$\varepsilon_p = (\delta^{13}C_{wax} + 1)/(\delta^{13}C_{CO2} + 1) - 1 \qquad (1)$$

$$\delta^{13}C_{wax,corr} = (\varepsilon_p + 1)(\delta^{13}C_{CO2,PI} + 1) - 1 \qquad (2)$$

The effect of the δ13C$_{CO2}$ corrections on the data is shown in Supplementary Fig. 3 and reported in Supplementary Table 5.

Corrections for oceanic δD variability. Changes in ice volume over time affect the isotopic composition of seawater and thus rainfall, which in turn is recorded by δD$_{wax}$ in lipid biomarkers such as those produced by plants. We correct for changes in the seawater isotopic composition by using a compilation of global benthic foraminifera δ18O values, which records changes in ice volume and deep-sea temperatures over time. We created a composite stack of benthic foraminifera δ18O values by splicing the LR04 stack (0–5.3 Ma)[51] into the stack from ref. [52] smoothed with a moving 0.25 Myr window (5.3–34.5 Ma). We adjust the stack by calculating anomalies relative to the modern value and then scaling the stack by the change in oceanic δ18O due to ice volume during the last glacial maximum (1.0‰; ref. [53]) divided by the change in the benthic δ18O anomaly from the same time interval (~1.5‰). These scaled anomalies are an estimate for the anomaly in the oxygen isotope composition of seawater (Δδ18O$_{sw}$). We calculate the seawater δD anomaly (ΔδD$_{sw}$) from the Δδ18O$_{sw}$ anomaly using the 8:1 relationship between δD and δ18O in modern precipitation. The ΔδD$_{sw}$ anomalies are linearly interpolated at sample ages, and ice volume-corrected δD$_{wax}$ values (δD$_{wax,IVC}$) were calculated using the equation:

$$\delta D_{wax,IVC} = (\delta D_{wax} + 1)/(\Delta\delta D_{sw} + 1) - 1 \qquad (3)$$

The effect of these corrections on the original data is shown in Supplementary Fig. 4 and reported in Supplementary Table 5.

The age models for Site 659 have sufficiently small uncertainties that exact ages were used to interpolate the seawater δD anomaly. The age models for sites 959, 235 and 241 have uncertainties large enough that estimates for the δD anomaly of seawater during the Pleistocene glacial/interglacial cycles could be substantially in error. To account for the age model uncertainty, we used a 0.15 Myr window centred on each age and take the mean of the minimum and maximum ΔδD$_{sw}$ anomaly in this window.

Calculation of the C₄ vegetation fraction. We calculate the fractional contribution of C₄ vegetation to each plant-wax *n*-alkane homologue using endmembers determined from modern African plant datasets tabulated by ref. [54]. We recalculated the endmembers using an atmospheric δ13C value of −6.5‰ (Supplementary Fig. 5) and used the All Africa endmembers in all manuscript figures and calculations. For comparison, we also separately show the δ13C values of savannah plants, rainforest plants and grasses (Supplementary Fig. 5). Fractional contributions were calculated from the measured δ13C value of a homologue (δ13C$_{wax}$, corrected for variations in atmospheric δ13C) assuming linear mixing, between the endmembers for that homologue (δ13C$_{C3}$, δ13C$_{C4}$):

$$f_{C4} = (\delta^{13}C_{wax} - \delta^{13}C_{C3})/(\delta^{13}C_{C4} - \delta^{13}C_{C3}) \qquad (4)$$

Other approaches have been applied to calculate the contribution or coverage of C₄ vegetation from leaf-wax δ13C values[54]. We take the linear mixing approach here as it directly estimates the f_{C4} of the leaf-waxes themselves, which we use in the calculation of hydrogen isotope fractionation factors.

Vegetation, landscape apparent fractionation and calculation of precipitation δD. To calculate precipitation δD (δD$_{ppt}$) from plant-wax δD values it is necessary to apply a fractionation factor that depends broadly on the plant-waxes contributed by each plant functional type to a sample. Here we reconstruct plant functional types using f_{C4} calculated from *n*-alkane homologues as an indicator for changing mixtures of endmember vegetation groups. The first endmember is based on the modern distributions of plant types. The modern savannah and xeric shrubland vegetation in west and east Africa consists of a mixture of C₄ grasses, C₃ savannah trees and C₃ shrubs. In Northwest Africa (Site 659) and off East Africa (sites 235 and 241) the modern f_{C4} is between 50 and 75%, based on the δ13C of the C₃₁ *n*-alkane (see the f_{C4} axes in Fig. 2a–c). Xeric shrubs and savannah trees are the likely sources for the modern C₃ vegetation. Vegetation endmember 1 is modelled as 80% C₄ grass and 20% C₃ shrub on the basis of these observations (Supplementary Table 6). The second endmember is based on palaeobotanical evidence. The few existing data on early and middle Miocene vegetation in Northwest Africa (Supplementary Discussion 2.2) suggest a dominantly open woodland with C₃ grasses commonly present. Vegetation endmember 2 in vegetation scenario 1 is therefore modelled as 90% C₃ angiosperm tree and 10% C₃ grass on the basis of this evidence. Reflecting the range of grass abundances in middle Miocene vegetation, we increased the C₃ grass abundance to 20% in vegetation scenario 2. The vegetation scenarios are further discussed in Supplementary Methods 1.3, reported in Supplementary Table 6, and shown in Supplementary Figs. 6–8.

The δD of plant-wax molecules is related to δD$_{ppt}$ through an empirical factor (termed the apparent fractionation; ε_a) that depends on plant type and, to a lesser extent, aridity[55]:

$$\varepsilon_a = (\delta D_{wax} + 1)/(\delta D_{ppt} + 1) - 1 \qquad (5)$$

To reconstruct δD$_{ppt}$ from plant-wax δD, it is necessary to apply a plant-type-specific ε_a to the dataset, which requires broad knowledge of the plant types and the proportions contributing plant-waxes to each sample.

The proportion of different plant types for each sample is used to calculate a landscape ε_a value by averaging each plant type's apparent fractionation value ($\varepsilon_{a,i}$) weighted by their relative proportion (w_i) from the vegetation reconstructions:

$$\varepsilon_{a\_landscape} = \sum w_i \varepsilon_{a,i} \qquad (6)$$

The apparent fractionation values for each plant type were calculated from the compilation of ref. [55] and are listed in Supplementary Table 6. The $\varepsilon_{a\_landscape}$ values and resulting δD$_{ppt}$ values for each site are shown in Supplementary Figs. 6–8 and reported in Supplementary Data 5. Qualitatively, the trend (or lack of trend) in water δD values through time is similar between scenarios. The maximum difference in δD$_{ppt}$ values between scenarios is ~5.2‰.

Comparison of Pleistocene and Neogene δD$_{ppt}$ variability. It seems that the range of variability in the δD$_{ppt}$ at Site 659 is similar to the orbital-precession-paced variability for the late Pleistocene (ice volume-corrected range of 35‰, 0–0.12 Ma)[35] (Fig. 2d) and Pliocene (ice volume-corrected range of 36‰)[36] at Site 659. To confirm this observation, we tested whether the Neogene variability is statistically similar to the late Pleistocene variability by comparing the distributions of δD$_{ppt}$ values. We used δD$_{ppt}$ values for the Neogene Site 659 from our study compared to late Pleistocene δD$_{ppt}$ values from ref. [35] that we recalculated with the same methodologies (vegetation correction using scenario 1, δ13C of atmosphere and δD of seawater). We used a Monte Carlo approach, resampling

the late Pleistocene dataset 1,000 times with a sample size equal to the Neogene dataset ($n = 20$). We treat the late Pleistocene values as a continuous function and randomly sample its cumulative distribution by interpolation using a polynomial cubic hermite interpolant.

The question we asked is whether the variability of the Neogene δD_{ppt} values is statistically different from that of the late Pleistocene δD_{ppt} data. We used the Monte Carlo resampled datasets to calculate quantiles at 2% intervals from 2 to 98% and, for each quantile, calculate the 95% range of the resampled data. We visualized the comparison of the Neogene and late Pleistocene data on a quantile–quantile (Q–Q) plot that has the advantage of effectively dealing with non-normal distributions. On a Q–Q plot, two datasets with identical means and distributions plot along a 1:1 line, whereas samples with different means but identical distributions plot along a line of slope 1 offset from the 1:1 line by the difference in their means. Datasets with different distributions diverge from a line of slope 1. The Q–Q plot of the Neogene versus late Pleistocene data is shown in Supplementary Fig. 9. The data plot close to a line of slope 1 that is offset from the 1:1 line by ~10 ‰, suggesting that the two datasets have similar variability but slightly different mean values. The slope = 1 line falls completely within the 95% range of the resampled late Pleistocene data, indicating no statistically significant difference in variability between the two datasets.

Direct evidence for orbitally paced precipitation in Northwest Africa only extends to ~10 Ma (refs. [56,57]), but based on this analysis and recent modelling work[58] it seems that orbital insolation has been a major regulator of North African climate since the Middle Miocene (~16–14 Ma), when the Arabian Peninsula neared its present geographic position (Supplementary Discussion 2.4).

We do not have comparable Pleistocene datasets to compare with the Neogene δD_{ppt} variability at sites 959, 235 and 241. However, on the basis of the analysis for Site 659, we suggest that the variability of δD_{ppt} at these other sites largely reflects persistent orbital-scale variations throughout the Neogene. Supporting this, the range of variability at sites 235 and 241 is similar to that present in orbital-scale records from the Gulf of Aden[59] and the eastern Mediterranean[60]. This interpretation of the variability is supported by our analysis below, which demonstrates no long-term trends in δD_{ppt} values. Thus, the variability present in the records must largely reflect the random sampling of a stationary process such as orbital variability, whose effects on δD_{ppt} have not changed enough to be detectable in our records.

Tests for trends in Neogene δD_{ppt}. Qualitatively, there does not seem to be a trend in the δD_{ppt} values at Site 659 or sites 235/241, whereas there may be a small trend at Site 959 (Fig. 2). Here we test whether any significant trends in δD_{ppt} with sample age exist in our data, across the different vegetation scenarios used to calculate δD_{ppt} values from δD_{wax} values, and across drilling sites from the three regions. We restricted the analysis to samples younger than 16 Ma to isolate trends immediately before and during expansion of C$_4$ vegetation. We evaluated significance with two methods. The first fits a line to the δD_{ppt} values versus sample age and determines the probability that the slope of the line is significantly different from zero using the t-test included in MATLAB's fitlm.m function. The second method uses a Monte Carlo approach, resampling each δD_{ppt} dataset 5,000 times (as described in the last section) and calculating slopes from the resampled data. The actual age–δD_{ppt} slope of the Neogene δD_{ppt} dataset is then compared with the distribution of slopes from the resampled data, and the percentile of the actual slope in the distribution of resampled data slopes is computed. To determine the probability that the actual slope arose by chance from sampling a stationary process whose variability is equal to the measured data, the percentile of the actual slope in the data is compared to the 95% and 99% confidence intervals of the slopes in the resampled data. The age–δD_{ppt} slopes for the different vegetation scenarios and datasets are plotted on top of the data in panel D of Supplementary Figs. 6–8, while the measured slopes and the distribution of slopes from the resampled datasets are shown in Supplementary Fig. 10. Each panel in Supplementary Fig. 10 also includes a P value from the t-test (P), and the percentile of the slope in the cumulative distribution of the resampled slopes (q).

We find that the slope of δD_{ppt} with time at Site 659 is small and not significantly different from zero in any of the more realistic vegetation scenarios that include C$_3$ grasses (scenarios 1 and 2, Supplementary Fig. 10). This analysis indicates that there is no detectable change in δD_{ppt} with time at this site. At sites 235/241, the slope is small and not different from zero in vegetation scenarios 1 and 2. Therefore, we also conclude that it is highly unlikely a true change in δD_{ppt} occurred at these sites. At Site 959, the slope is consistently positive (decreasing δD_{ppt} from the Miocene to present) and significantly different from zero in both vegetation scenarios 1 and 2. The positive slopes are largely driven by the three negative data points younger than 5 Ma. We cannot exclude the possibility that some change in δD_{ppt} may have occurred at Site 959. Further analyses of samples younger than 5 Ma would confirm this finding. However, from the data it seems that this change at Site 959 post-dates the onset and major phase of C$_4$ expansion in Northwest and East Africa. There is therefore no compelling evidence of δD_{ppt} change at Site 959 accompanying the onset of C$_4$ vegetation expansion at 10.5 Ma.

Dust flux at Site 659. We calculated a new record of dust flux to Site 659 from a compilation of published compositional data and our revised age model. The

sediments at Site 659 are a mixture of terrigenous sediments dominated by aeolian dust[41] and biogenic carbonates. We compiled calcium carbonate (%CaCO$_3$) and dry bulk density (DBD) data from published and shipboard measurements[42,61,62]. We determined the linear sedimentation rate (LSR) with linear interpolation. We further smoothed the rapid sedimentation rate changes of the past 5 Myr from the astronomically tuned age model to make them comparable in spacing and rate of change to those from nannofossil datums deeper in the core. The age–depth data were smoothed with a moving linear least-squares fit with a 0.5 Myr window and the LSR calculated from the slope of the least-squares line. Dust flux was calculated as:

$$\text{dust flux}\ (\text{g cm}^{-2}\ \text{kyr}^{-1}) = (1 - \%\text{CaCO}_3/100) \times \text{LSR} \times \text{DBD} \qquad (7)$$

We then calculated median and the 10 and 90% quantiles of the dust flux data in overlapping 1 Myr bins, which are plotted over the data in Fig. 3. Raw and smoothed dust fluxes are reported in Supplementary Table 7.

Calculation of Neogene SST anomalies. The long-chain alkenone SST records of ref. [29] were reanalysed here to calculate SSTa values in different latitude bands (Fig. 3a). First, the SSTa for each site was determined by calculating the SST difference between the measured temperatures and the modern ocean temperature at the past latitude and longitude of the site. Each SSTa record was then averaged in overlapping 0.250 Myr bins to create a record that filters out orbital variability and captures long-term trends. Sites were then grouped by latitude and SSTa averaged across grouped sites to create the SSTa records in Fig. 3b.

Data availability
All data presented in this paper are freely available in Supplementary Tables 1–7.

References

37. Ruddiman, W. F., Sarnthein, M., Baldauf, J. & Shipboard Scientific Party *Proceedings of the Ocean Drilling Program: Initial Reports* Vol. 108 (Ocean Drilling Program, 1988).
38. Ruddiman, W. F. et al. Late Miocene to Pleistocene evolution of climate in Africa and the low-latitude Atlantic: overview of Leg 108 results. In *Proceedings of the Ocean Drilling Program: Scientific Results* Vol. 108 (eds Ruddiman, W. F. et al.) 463–484 (Ocean Drilling Program, 1989).
39. Mascle, J., Lohmann, G. P., Clift, P. D. & Shipboard Scientific Party *Proceedings Ocean Drilling Program: Initial Reports* Vol. 159 (Ocean Drilling Program, 1996).
40. Tiedemann, R. *Acht Millionen Jahre Klimageschichte von Nordwest Afrika und Paläo-Ozeanographie des angrenzenden Atlantiks: Hochauflösende Zeitreihen von ODP-Sites 658-661*. PhD thesis, Christian-Albrechts-Univ. Kiel (1991).
41. Tiedemann, R., Sarnthein, M. & Shackleton, N. J. Astronomic timescale for the Pliocene Atlantic δ^{18}O and dust flux records of Ocean Drilling Program Site 659. *Paleoceanography* **9**, 619–638 (1994).
42. Shipboard Scientific Party. Site 659. In *Proceedings Ocean Drilling Program: Initial Reports* Vol. 108 (eds Ruddiman, W. F. et al.) 221–325 (Ocean Drilling Program, 1988).
43. Weaver, P. P. E. et al. Biostratigraphic synthesis: Leg 108, Eastern Equatorial Atlantic. In *Proceedings of the Ocean Drilling Program: Scientific Results* Vol. 108 (eds Ruddiman, W. F. et al.) 455–462 (Ocean Drilling Program, 1989).
44. Shipboard Scientific Party. Site 959. In *Proceedings Ocean Drilling Program: Initial Reports* Vol. 159 (eds Mascle, J. et al.) 65–150 (Ocean Drilling Program, 1996).
45. Wade, B. S., Pearson, P. N., Berggren, W. A. & Pälike, H. Review and revision of Cenozoic tropical planktonic foraminiferal biostratigraphy and calibration to the geomagnetic polarity and astronomical time scale. *Earth-Sci. Rev.* **104**, 111–142 (2011).
46. Backman, J., Raffi, I., Rio, D., Fornaciari, E. & Pälike, H. Biozonation and biochronology of Miocene through Pleistocene calcareous nannofossils from low and middle latitudes. *Newsl. Stratigr.* **45**, 221–244 (2012).
47. Raffi, I. et al. A new low-to middle-matitude biozonation and revised biochronology of Palaeogene calcareous nannofossils. In *STRATI 2013: The First International Conference on Stratigraphy* (eds Rocha, R. et al.) 137–141 (Springer Geology, 2014).
48. Polissar, P. J. & D'Andrea, W. J. Uncertainty in paleohydrologic reconstructions from molecular δD values. *Geochim. Cosmochim. Acta* **129**, 146–156 (2014).
49. Tipple, B. J., Meyers, S. R. & Pagani, M. Carbon isotope ratio of Cenozoic CO$_2$: a comparative evaluation of available geochemical proxies. *Paleoceanography* **25**, PA3202 (2010).
50. Francey, R. J. et al. A 1000-year high precision record of δ^{13}C in atmospheric CO$_2$. *Tellus B* **51**, 170–193 (1999).
51. Lisiecki, L. E. & Raymo, M. E. A Pliocene-Pleistocene stack of 57 globally distributed benthic δ^{18}O records. *Paleoceanography* **20**, PA1003 (2005).
52. Zachos, J. C., Dickens, G. R. & Zeebe, R. E. An early Cenozoic perspective on greenhouse warming and carbon cycle dynamics. *Nature* **451**, 279–283 (2008).

53. Schrag, D. P. et al. The oxygen isotopic composition of seawater during the last glacial maximum. *Quat. Sci. Rev.* **21**, 331–342 (2002).

54. Garcin, Y. et al. Reconstructing C_3 and C_4 vegetation cover using n-alkane carbon isotope ratios in recent lake sediments from Cameroon, Western Central Africa. *Geochim. Cosmochim. Acta* **142**, 482–500 (2014).

55. Sachse, D. et al. Molecular paleohydrology: interpreting the hydrogen-isotopic composition of lipid biomarkers from photosynthesizing organisms. *Annu. Rev. Earth Planet. Sci.* **40**, 221–249 (2012).

56. Schenau, S. J. et al. Organic-rich layers in the Metochia section (Gavdos, Greece): evidence for a single mechanism of sapropel formation during the past 10 My. *Mar. Geol.* **153**, 117–135 (1999).

57. Larrasoaña, J. C., Roberts, A. P. & Rohling, E. J. Dynamics of green Sahara periods and their role in hominin evolution. *PLoS ONE* **8**, e76514 (2013).

58. Zhang, Z. et al. Aridification of the Sahara desert caused by Tethys Sea shrinkage during the Late Miocene. *Nature* **513**, 401–404 (2014).

59. Tierney, J. E., deMenocal, P. B. & Zander, P. D. A climatic context for the out-of-Africa migration. *Geology* **45**, 1023–1026 (2017).

60. Rose, C., Polissar, P. J., Tierney, J. E., Filley, T. & deMenocal, P. B. Changes in northeast African hydrology and vegetation associated with Pliocene-Pleistocene sapropel cycles. *Phil. Trans. R. Soc B* **371**, 20150243 (2016).

61. Stein, R., ten Haven, H. L., Littke, R., Rullkötter, J. & Welte, D. H. Accumulation of marine and terrigenous organic carbon at upwelling Site 658 and nonupwelling Sites 657 and 659: implications for the reconstruction of paleoenvironments in the eastern subtropical Atlantic through late Cenozoic times. In *Proceedings Ocean Drilling Program: Scientific Results* Vol. 108 (eds Ruddiman, W. F. et al.) 361–385 (Ocean Drilling Program, 1989).

62. Tiedemann, R., Sarnthein, M. & Stein, R. Climatic changes in the Western Sahara: aeolo-marine sediment record of the last 8 million years (Sites 657-661). In *Proceedings of the Ocean Drilling Program: Scientific Results* Vol. 108 (eds W. F. Ruddiman et al.) 241–277 (Ocean Drilling Program, 1989).